Chapter

Metallo-Dielectric Colloidal Films as SERS Substrate

Ana L. González, Arturo Santos Gómez and Miller Toledo-Solano

Abstract

Along this chapter, we probe that the discrete dipole approximation models fairly well the optical response of periodic systems. Herein, we use it to model the reflectance and transmittance, at normal incidence, of colloidal films made of SiO_2 spheres. As the thickness increases from 1 to 12 layers, the photonic band gap shifts to the blue tending to the value corresponding to a 3D opal, 442 nm. A film with more than eight layers resembles the bulk properties of a 3D opal. Our results are compared to a real sample. Besides, we show that taking advantage of the wide and asymmetrical absorbance spectrum of an opal with Au NPs is possible to identify the contribution of each component in the overall spectrum, through a deconvolution analysis. Finally, we present the electric field intensity as the content of metal NP increases in a monolayer. We consider NPs one order of magnitude smaller than the silica spheres, and then, 6, 9, and 17 NPs are hosted in the void. Similar average electric field intensities, about 11 times the incident intensity, are obtained with Au and Ag NPs. But, the spots with these intensities cover a bigger area with Ag NPs than with Au NPs.

Keywords: metal nanoparticles, SiO_2 spheres, colloidal thin films, discrete dipole approximation, photonic band gap, near field intensity

1. Introduction

A crystal is defined as the solid formed by a long range periodic array of atoms or molecules. Its periodic lattice originates a potential with the same periodicity, and as outcome, the energy levels give rise to allowed and forbidden bands. In consequence, the physical properties of crystals depend on the band structure. For instance, an electromagnetic wave with a frequency in the interval of the forbidden band will be reflected or absorbed by the crystal. In nature, other entities instead of atoms or molecules can conform to ordered arrangements. For example, Tobacco mosaic virus is a virus that infects plants, especially tobacco plant (where its name comes from); it has a rod-shape with the ability of self-assembling naturally creating a bi-dimensional triangular structure. This assembly has been exploited to increase the capacity of batteries [1] and as a template for the fabrication of functional devices [2]. Other periodic structures, found in nature or produced artificially, are the named colloidal crystals. A colloidal crystal is an assembly of colloid particles with a periodic structure. Its bulk properties depend on composition,

particle size, and packing arrangement. Opals are an example of colloidal crystals, in nature and under specific conditions of pressure and temperature; silicon dioxide (SiO_2) spheres accommodate in a close-packed array. Probably its most well-known optical property is the constructive interference of light either at its surface or interior producing certain colors as the angle of incident light changes, and this property is named iridescence.

Artificially, opals can be formed in a liquid medium or during drying/evaporation of particle suspension. Nowadays, it is possible to synthesize them with dielectric spheres of porous silica, polymethyl methacrylate, polystyrene, and others, of diameter of hundreds of nanometers. The main impressive characteristic of artificial opals is its optical response in the visible range [3, 4], and this has technological implications that place them as photonic band gap (PBG) materials. A bidimensional ordered array (thin film) can be used as coatings of several substrates, allowing to optimize or even modify some of the physical and chemical properties of the substrate. Its optical response may depend on the geometry of the periodic array, defects, and thickness. Some artificial opals have been reported with a face centered cubic (FCC) or close-packed hexagonal (HCP) structure with sequences ABCABC and ABAB, respectively [5, 6].

On the other hand, nanocomposite materials often exhibit exceptional properties compared to their constituents. Consequently, the incorporation of metal nanoparticles (NPs) into colloidal crystals is a subject of study that emerges naturally [7]. Some of the methods to achieve the incorporation of the NPs are based on self-assembling, electroplating process, and photolysis [8–10]. The applications of these composite thin films cover catalysis, optical devices, solar cell, and sensors [11–15], among others.

Particularly, composite periodic structures constructed by using colloidal crystals as templates and Au NPs have been tested as surface enhanced Raman scattering (SERS) substrates. These SERS substrates are simple and inexpensive to prepare and, moreover, offer the benefit of being highly stable. However, the SERS enhancement factor (EF) depends on several factors such as the probe molecule, concentration and shape of Au NPs, and thickness of the substrate. One may think that only the NPs in the top layer of the thin film are illuminated by the excitation laser and hence contribute to the SERS signal [16]. Nevertheless, larger SERS signal has been detected using thin composite substrates (less than 10 silica layers) rather than thick ones (more than 10 silica layers), and more surprising is the fact that the SERS enhancement falls down when substrates with a thickness between 1 and 2 mm are used [17]. Therefore, it seems that the SERS EF is thickness dependent, but the origin of this behavior is not completely understood.

This chapter is dedicated to the study of the optical response of colloidal thin films (multilayers of SiO_2 spheres), with and without metal nanoparticles. In Section 2, we briefly describe the discrete dipole approximation method to model the reflectance (R), transmittance (T), and near electric field intensity. Section 3 contains an analysis of R and T of colloidal thin films as the thickness increases from 1 to 12 layers of SiO_2 spheres. Section 4 focuses on a composite thin film and its role as SERS substrate; first, the absorbance spectra are proposed as a tool to verify the inclusion of Au NP, and second, the near electric field intensity as the amount of Au NP increases is shown.

2. Discrete dipole approximation for periodic targets

Nowadays, there are several methods with their respective numerical implementations to enquire into the optical response of single targets, one of them

is the discrete dipole approximation (DDA). This method has been widely used to study the absorbed and scattered light of several systems and materials as nanoparticles, human blood, bacteria, and interstellar dust, among others [18–23]. Herein, we place attention to DDA's extended version, proposed by Draine and Flatau, for modeling R and T of infinite 2D periodic systems [24]. Recently, DDA was employed to study R and T of periodic arrays of dielectric and metal spheres [25].

In **Figure 1**, a section of a bi-dimensional periodic array of solid spheres is exemplified, each one discretized by N_{dip} dipoles represented by tiny spheres. As an analogy of atoms in a solid crystalline structure, the definition of a convenient unit cell is helpful. The target unit cell (TUC) is the entity located at the origin and that is repeated along the yz plane with an L_y and L_z periodicity. (m,n) is a pair of integers that defines the position of the TUC's replica at m units along the y axis and n units along the z axis.

The position and dipole moment of the dipole j of the (m,n) TUC replica are expressed as

$$\mathbf{r}_{jmn} = \mathbf{r}_{j00} + m\mathbf{L}_y + n\mathbf{L}_z, \tag{1}$$

$$\mathbf{p}_{jmn} = \mathbf{p}_{j00} \exp\left[i\left(m\mathbf{k}_0 \cdot \mathbf{L}_y + n\mathbf{k}_0 \cdot \mathbf{L}_z\right)\right] \qquad \text{for each } j = 1, \ldots, N_{dip}, \tag{2}$$

$\mathbf{L}_y$ and $\mathbf{L}_z$ are the vectors that define the periodicity of the array; $\mathbf{r}_{j00}$ is the position vector of the j dipole that belongs to the TUC (the one at the origin), and $\mathbf{k}_0$ is the incident wave vector.

The dipole moment $\mathbf{p}_{j00}$ of the j dipole in the TUC satisfies the equation

$$\mathbf{p}_{j00} = \overleftrightarrow{\alpha}_j \cdot \left[\mathbf{E}_{\text{inc}}(\mathbf{r}_j) - \sum_{k \neq j} \tilde{\mathbf{A}}_{j,k}\mathbf{p}_{k00}\right], \tag{3}$$

where $\overleftrightarrow{\alpha}_j$ is the polarizability tensor, $\mathbf{E}_{\text{inc}}(\mathbf{r}_j)$ is the field of an incident plane wave at the position $\mathbf{r}_j$, and $\tilde{\mathbf{A}}_{j,k}$ is a matrix that takes into account the interaction

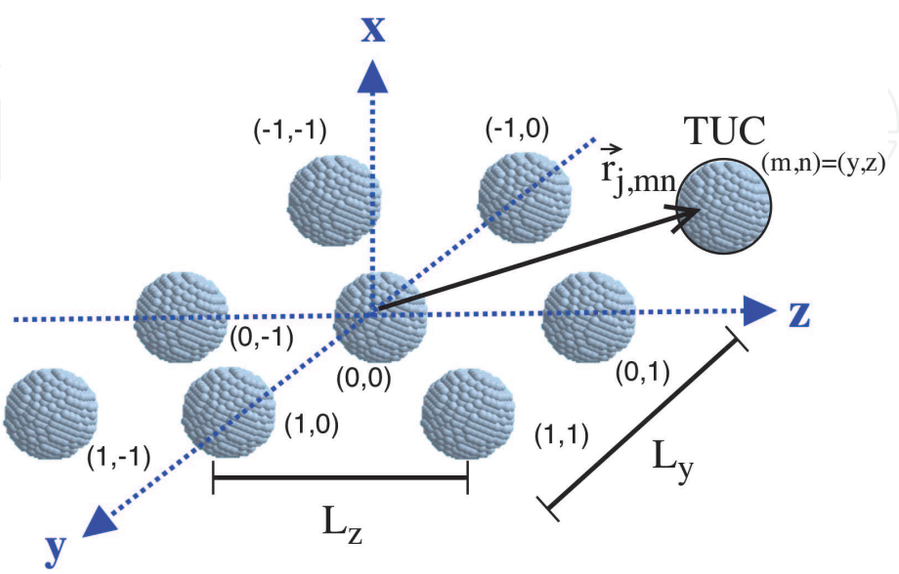

Figure 1.
A section of an infinite bidimensional periodic array of spheres. Each sphere is discretized by an array of N_{dip} dipoles. $\mathbf{r}_{j,mn}$ is the position of the j dipole of the target unit cell (TUC) replica located at m units along the y axis and n units along the z axis. Figure taken with permission from Ref. [25].

between the dipole located at $\mathbf{r}_{j00}$ and the field induced by the dipoles of the TUC and its replicas at the $\mathbf{r}_{kmn}$ positions; for more details, see [24].

If there are N_{dip} dipoles in the TUC with a similar equation to Eq. (3) existing for each dipole, then, a system of $3N_{dip}$ complex coupled equations needs to be solved for $\mathbf{p}_{j00}$ values. Once the equation system is solved, then far and near field optical response of the periodic target can be calculated.

Usually, N_{dip} dipoles are of the order of $10^5 - 10^6$; hence, numerical tools are necessary to solve the system of $3N_{dip}$ equations. A robust numerical implementation of DDA is the DDSCAT code [26] that assumes an incident plane wave along the positive direction of x axis and a bidimensional target resting on the yz plane. Among other interesting physical quantities, the 2×2 scattering amplitude matrix elements S_i can be calculated, and consequently, the 4×4 scattering intensity matrix elements $S_{\alpha\beta}$ [27].

For the specific case of unpolarized incident light, R and T are related to the $S_{\alpha\beta}$ elements through the next expressions:

$$R = S_{11} \quad \text{for } (k_{sx}k_{0x} < 0), \tag{4}$$

$$T = S_{11} \quad \text{for } (k_{sx}k_{0x} > 0), \tag{5}$$

where k_{sx} and k_{0x} are the wave vector components of the scattered light and of the incident light, respectively. Both of them are along the direction of the incident light. The S_{11} value is related to S_i elements by:

$$S_{11} = \frac{1}{2}\left(|S_1|^2 + |S_2|^2 + |S_3|^2 + |S_4|^2\right). \tag{6}$$

3. Colloidal films of SiO_2 spheres: effect of thickness

This section is devoted to the effect of thickness of a colloidal film on its optical response. We consider a film built by N layers made of SiO_2 spheres with a diameter of 200 nm, ordered in HCP structure (AB sequence). A scheme of the thin film is shown in **Figure 2**; there, the film is on the yz plane and its thickness goes along the x axis. Also, the incident electromagnetic (EM) plane wave has a wave vector **K** in direction of the positive x axis.

The TUC for each N layer thin film, with N from 1 to 12, is conveniently built. The TUC for the monolayer contains two spheres, for the bilayer four spheres, for

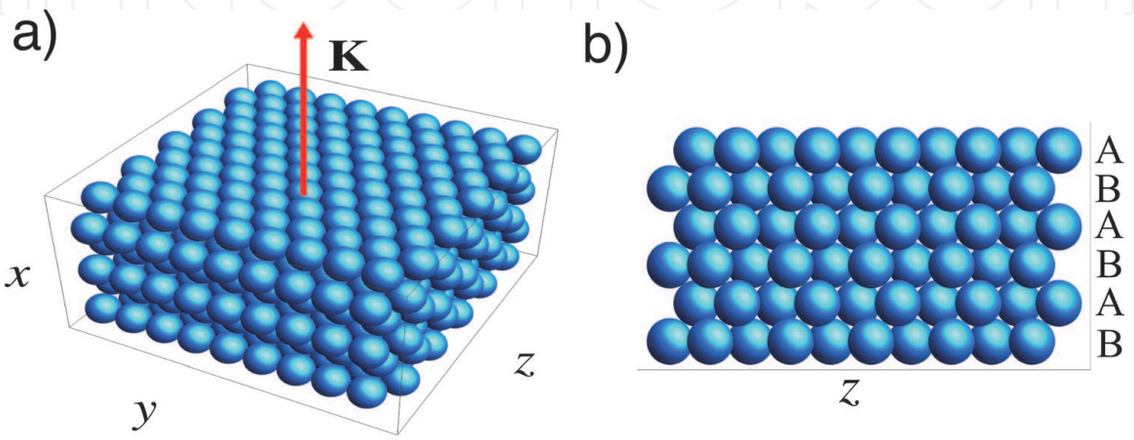

Figure 2.
*(a) The wave vector **K** of the incident EM plane wave, perpendicular to the thin film. (b) Lateral view of a thin film composed of 6 layers of SiO_2 spheres in an ABAB sequence.*

the three-layer six spheres, and so on. A 10 nm separation distance between two adjacent dipoles is used, implying about 4600 dipoles per sphere.

In the visible range, the refractive index of the silica, n_{SiO_2}, is almost constant, and its variations go from 1.48 to 1.45 for wavelengths from 400 to 700 nm [28, 29]. For simplicity and without loss of information, we choose $n_{SiO_2}(\lambda) = 1.46$. It is noteworthy to mention that in the visible the imaginary part of n_{SiO_2} is negligible compared to the real part. However, in the ultraviolet interval, special care needs to be taken as the imaginary part comes to be significant and it is associated to the absorption coefficient.

R and T of a thin film composed of N layers, when light comes parallel to the normal of the surface, are shown in **Figure 3**. As the number of layers increases from 1 to 12, that is, as the film becomes thicker, a maximum of R emerges defining a photonic band, getting sharper around 450 nm. The optical spectrum to the left and right of the PBG is not symmetric because we have chosen the wavelength as the independent variable and not the wave number. The thickness, wavelength of the BG center (λ_c), width of the BG (ΔBG), effective refractive index of the thin film (n_{eff}), and optical path length (L) of each thin film are given in **Table 1**. Each quantity is estimated as follows:

The thickness is determined by considering the diameter of the sphere, D, and geometrical aspects of the AB sequence, as is explained next. The base of a tetrahedron is formed by the center of three spheres on a layer A, its height goes from its base to the center of a sphere of layer B, and the last is resting on the void left by the three spheres on layer A. The height of the tetrahedron coincides with the separation distance, d(1 1 1), between two adjacent planes with Miller indices (1 1 1). Then, the thickness of a film with N layers is $(N-1)\text{d}(1\,1\,1) + D$, with $\text{d}(1\,1\,1) = \sqrt{(2/3}D$.

λ_c is extracted from the calculated R(λ) spectrum, noting that it moves to the blue as the thickness increases, stopping around 444 nm. Latter, we compare this stop value to the λ_c of a 3D opal, and with experimental results. ΔBG is associated to the full width at the half maximum (FWHM) of the spectrum, and to estimate it, a Gaussian centered at the Bragg peak (the maximum of the R spectrum) was

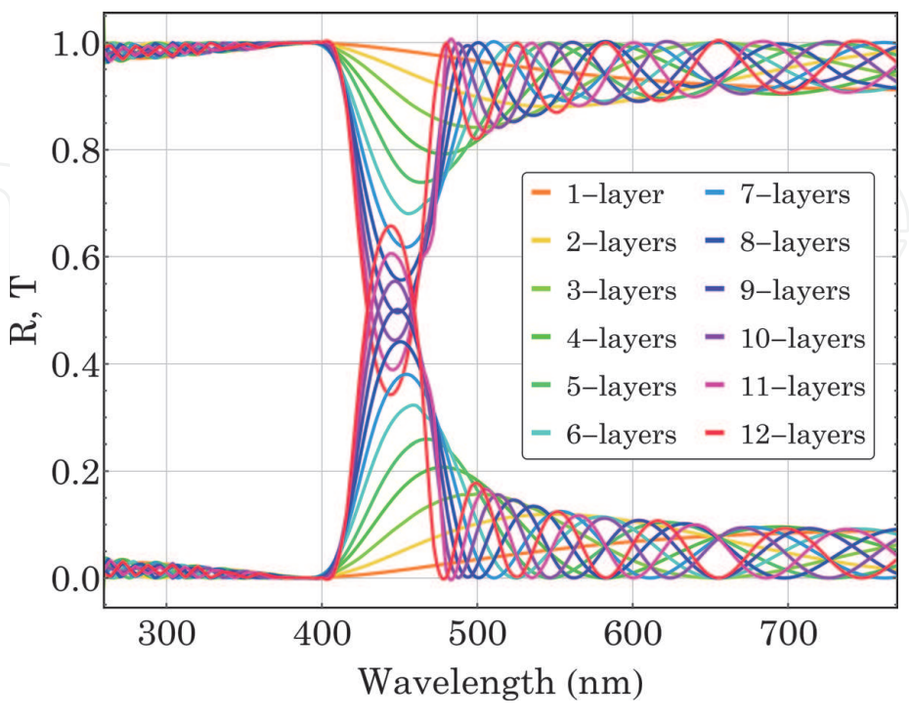

Figure 3.
Reflectance and transmittance of a thin film composed of N layers of 200 nm SiO_2 spheres. The incident light comes normal to the surface and is unpolarized.

Number of layers	Thickness (nm)	λ_c (nm)	ΔBG (nm)/(eV)	n_{eff}	L (nm)
1	200	650	—	1.29	251.9
2	363.3	549.7	—	1.3	211.4
3	526.4	499	—	1.33	187.6
4	689.9	476	—	1.34	177.6
5	853.2	465	73.64/16.7	1.34	173.5
6	1016.5	457	62.96/19.54	1.34	170.5
7	1179.8	453	55.39/22.21	1.35	169.0
8	1343.1	450	50.04/24.58	1.35	166.7
9	1806.4	449	46.05/26.71	1.35	166.3
10	1669.9.	447	43.28/28.42	1.35	165.5
11	1833.0	444.7	42.47/28.96	1.35	164.7
12	1996.3.	444.3	37.57/32.74	1.35	164.5

Table 1.
Thickness of the thin film composed of N layers, BG center position (λ_c), width of the BG (ΔBG), effective refractive index (n_{eff}), and optical path length (L).

adjusted. The trend is that the PB becomes narrow as the film is getting thicker. In **Table 1,** the ΔBG values are given in nm and eV.

Because the film is a heterogeneous material composed of SiO_2 spheres with air at the interspace, a refractive index can be assigned to it in order to treat the film as a homogeneous material with an effective property, n_{eff}. This can be done relating the refractive index of each involved material and its filling fraction (ff)[1], that is, the fraction of volume occupied by the spheres and air. n_{eff} is deduced using [30]:

$$n_{eff}^2(\lambda) = n_{air}^2(1 - ff) + n_{SiO_2}^2(\lambda)ff. \tag{7}$$

$n_{eff} = 1.35$ for more than seven layers (see **Table 1**), the same value of a 3D opal with HCP structure.

In the last column of **Table 1**, the optical path length (L) associated to the inhomogeneous thin film is determined simply using the generalized Bragg equation at normal incidence [31]:

$$L = \frac{\lambda_c}{2n_{eff}}, \tag{8}$$

L is interpreted as the path that follows the light when going through the heterogeneous film in order to produce constructive interference.

Now, Let's keep in mind the trend observed by the position of λ_c as the thickness of the film increases: a shift to the blue stopping at a value around 444 nm. On the other hand, consider a 3D opal with an HCP structure and a ff = 0.74. Then, using (Eq. 7) and generalized Bragg's law

$$\lambda_{c,opal} = 2d_{(111)}\sqrt{n_{eff}^2 - \sin^2\theta}, \tag{9}$$

[1] The ff is calculated considering a cell of a hexagonal base with a length side D and a high defined by the thickness of the N layers. Then, ff= mV_{sphere}/V_{cell}, with V_{sphere} and V_{cell} being the volume of a sphere and the cell, respectively. m is the number of spheres in the cell.

the wavelength of the center of the PBG, $\lambda_{c,opal}$, can be estimated. For the specific case of normal incidence and constructive interference due to planes (111), $\lambda_{c,opal}$ = 442.7 nm, a value very close to 444 nm. Then, the PBG of films with more than eight layers resembles that of a 3D artificial opal (see **Figure 4**). Excluding thin films with less than three layers, the best fitting for λ_c as a function of the number of layers is a polynomial of third order: $\lambda_c\,(N) = 600.57\,\text{nm} - 48.04\,N + 5.11\,N^2 - 0.18\,N^3$.

In **Figure 5**, the reflectance of an opal of 200 nm SiO_2 spheres has a PBG with a maximum around 474 nm [17], agreeing to our results shown in **Figure 3**. The

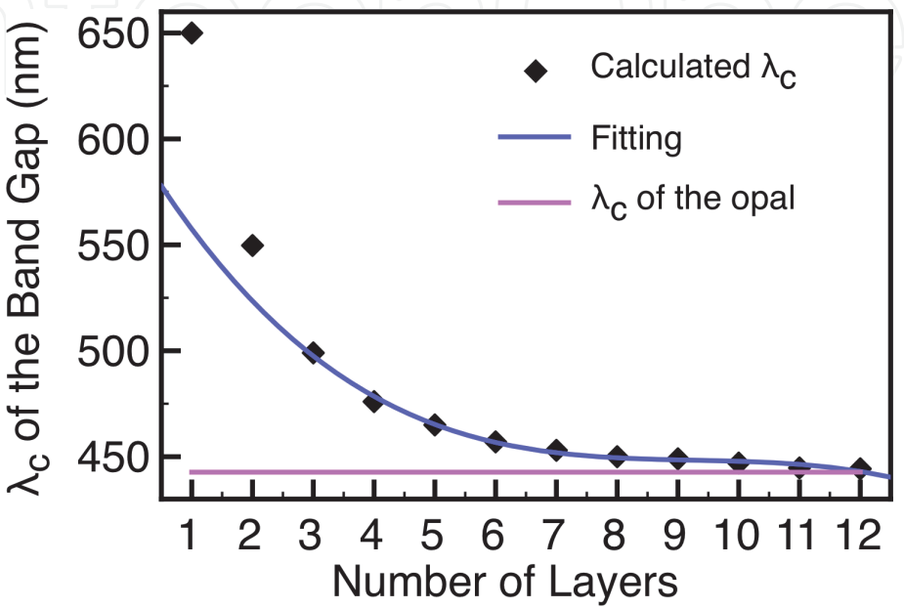

Figure 4.
Wavelength position of the center of the band gap, λ_c, as the number of layers increases. λ_c of a 3D opal is about 442.7 nm.

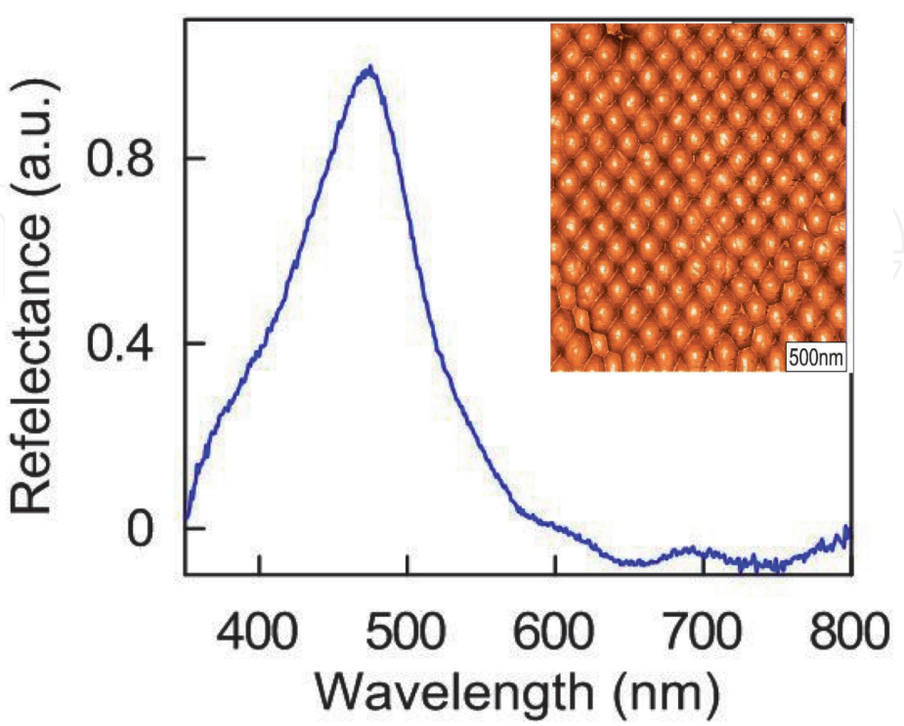

Figure 5.
Reflectance of an opal of 200 nm silica spheres; its PBG has a maximum around 474 nm. In the AFM image, some defects are noticed in the orderliness. Image modified with permission from Ref. [17].

asymmetry of the spectrum and difference in position of the gap center is presumably due to the presence of defects and polydispersity of the synthesized thin film.

4. Composite thin film: effect of metal NPs' concentration

Composite colloidal films are an option for having a substrate with the advantages of rough, periodic and plasmonic material. Its performance depends on the concentration, shape, and size of the metal NPs; type of probe molecule; and thickness of the film. Consequently, the large amount of variables involved makes difficult to establish the trend that may follow a good SERS substrate.

Au and Ag are the most plasmonic materials used to boost the SERS signal. However, it is easier to incorporate Au on crystal colloids than Ag. From the several interesting reports about the synthesis and characterization of composite colloidal thin films with Au, we can highlight the following aspects [7, 17, 32]:

- When the size of the plasmonic NPs is smaller than the size of the dielectric spheres, the lattice of the opal is not distorted.
- The photonic band of the composite shows a red shift, a reduction of its width and intensity upon increasing NP doping level.
- Even for large loads of Au NPs, evidence of the plasmon resonance is not noticeable in the reflectance spectrum of the composite.

4.1 Evidence of incorporation of metal NPs

Recently, we reported SERS-substrate films with the advantage of a rough surface provided by a periodic array of SiO_2 spheres and Au NPs [32]. The synthesis of colloidal SiO_2 spheres was performed following the methods of Stöber [33] and Razo [5], while Au NP colloid was prepared adopting the method introduced by Turkevich [34, 35]. The size of silica spheres and Au NPs is 275 and 22 nm, respectively. Besides, the surface plasmon resonance of the NPs is located at 522 nm (see Ref. [32]). The as-synthesized SiO_2 spheres and Au NPs were used to obtain composite films with low, medium, and high volume concentrations of Au NPs (composite 1, 2, and 3, respectively), accordingly to the procedure reported by Cong et al. [36], and that previously has been employed by some of us to prepare the opal/Fe_3O_4 colloidal crystal [37]. The films were deposited on a glass substrate, and to make evidence of their functionality as SERS substrates, methylene blue (MB) was employed as the molecular probe. An EF of the order of 10^5 was reached with the composite 3.

Figure 6(a) exhibits the surface of the SiO_2 opal where some internal planes are appreciated. Despite the presence of some vacancies, an FCC array is recognized. Scanning electron microscopy (SEM) image of composite 3 reveals that Au NPs are located at the interstitial sites (see **Figure 6(b)**). Moreover, the center-to-center distance between adjacent spheres in the composite is almost the same as that of the bare SiO_2 opal (panels (c) and (d) of **Figure 6**). Hence, the lattice of the opal is not distorted even using a relatively high volume concentration of Au NPs. As the concentration of Au NPs increases, more NPs cover the SiO_2 spheres and the consequent visual effect is SiO_2 spheres of smaller diameter (as it is well noticed in **Figure 6(b)**). A similar tendency has been perceived with nonspherical Au NPs, and at low concentrations, Au nanorods reside in the voids, but as the concentration increases, they start to cover the surface of the spheres [17].

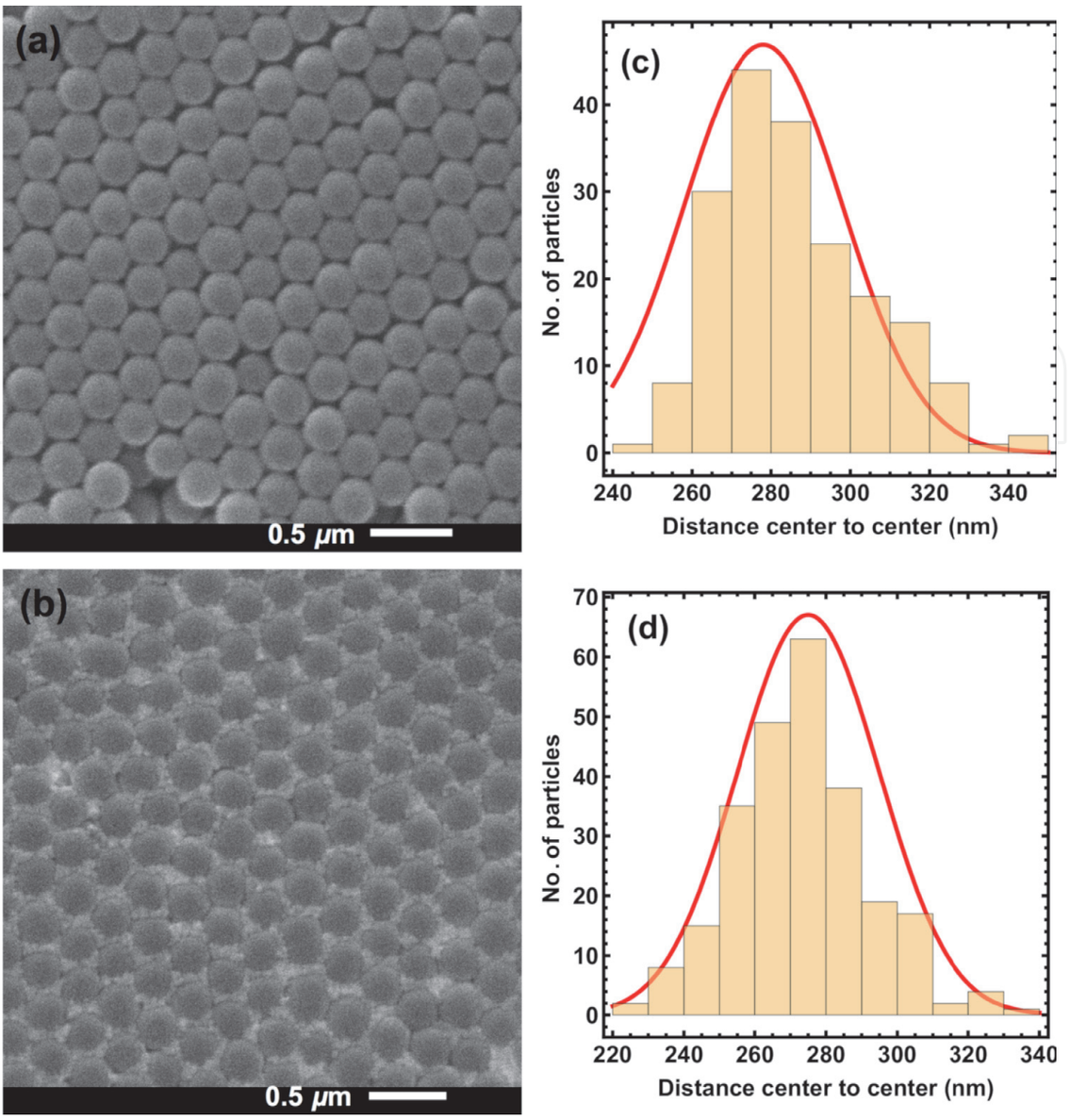

Figure 6.
Micrographs by SEM of films made of SiO_2 spheres before (a) and after infiltration of Au NPs (b). (c) and (d) show the center to center distance distribution histograms between adjacent spheres. The average distance corresponds to 278 ± 20 nm (opal) and 275 ± 20 nm, respectively. Image modified with permission from Ref. [32].

In **Figure 7**, UV–vis absorbance (A) spectrum of the films made of SiO_2 spheres before and after infiltration (composite 1, 2, and 3) is presented. The blue non–soft lines correspond to the measured spectra. For the opal, the peak is attributed to the PB, which originates from the diffraction of the 3D ordered structure of the colloidal crystal. With the naked eye, a wider and asymmetric spectrum of the composites compared to that of the opal is appreciated. To enquire the effect of each component of the composite on the overall spectrum, a deconvolution analysis may be carried out. Considering a Gaussian curve associated to the silica opal and other to the Au NPs, the general expression is of the form:

$$A(\lambda) = E + B_{\text{opal}} \exp\left(-(\lambda - \lambda_{\text{opal}})^2/2\sigma_{\text{opal}}^2\right) + C_{\text{Au}} \exp\left(-(\lambda - \lambda_{\text{Au}})^2/2\sigma_{\text{Au}}^2\right), \tag{10}$$

where E is a fitting value that moves the curve along the dependent variable axis; B_{opal} and C_{Au} are real values related to the highest point of each Gaussian curve;

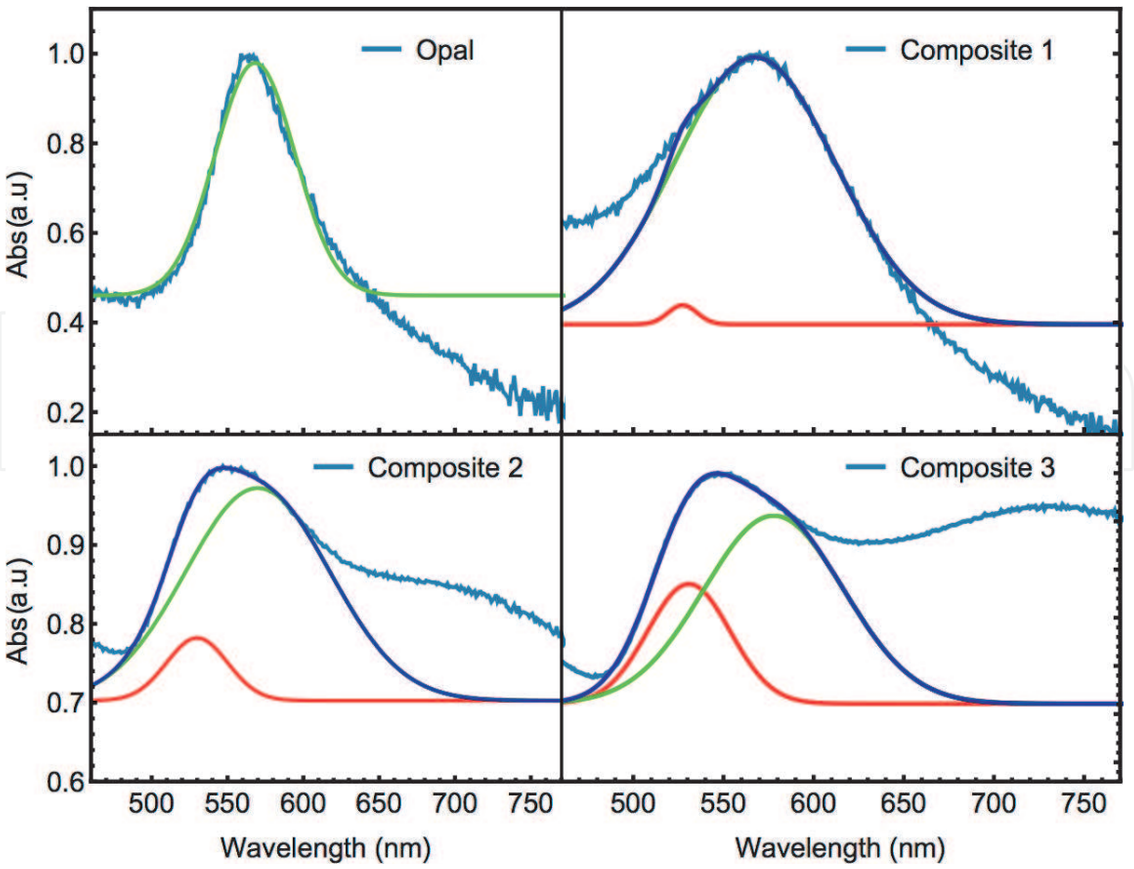

Figure 7.
UV–Vis absorbance spectrum of the films made of SiO_2 spheres before and after infiltration with low (composite 1), medium (composite 2), and high (composite 3) degree of Au NP loading. Blue non–soft line is the experimental measurement; red and blue lines are the Gaussian curves associated to the Au and silica arrays, respectively; blue soft line is the sum of blue and green lines.

Film	λ_{opal}	σ_{opal}	λ_{Au}	σ_{Au}
SiO_2	568 nm	26 nm		
Composite 1	567 nm	44 nm	527 nm	8 nm
Composite 2	570 nm	48 nm	530 nm	20 nm
Composite 3	578 nm	39 nm	532 nm	23 nm

Table 2.
Gaussian fitting parameters for absorbance bands.

λ_{opal} and λ_{Au} are the central wavelengths; and σ_{opal} and σ_{Au} are the respective FWHM. The corresponding fitting values are presented in **Table 2**. The addition of the two Gaussians give rise to a distribution (blue soft line) that fits the experimental distribution, see panels of **Figure 7**. The red and green lines are the Gaussian curves attributed to the contribution of Au and silica arrays in the composite, respectively.

SiO_2 film spectrum is very well adjusted to a Gaussian with a peak around 568 nm and a FWHM of 26 nm (see **Figure 7**). Meanwhile, when relatively low, medium, or high Au NPs concentration is incorporated in the opal, an asymmetrical and wide absorbance spectrum is noticed. At low concentration (composite 1), apparently still dominates the band assigned to the SiO_2 array and the outcome is a distribution with a slightly negative asymmetry. At medium (composite 2) and high (composite 3) concentration, it seems that the Au NP signal starts to predominate and the result is a distribution with a positive asymmetry.

As the concentration of Au NPs in the opal film increases, the center of the respective Gaussian curve (red line) is red shifted, compared to the surface plasmon resonance of the colloidal solution of Au NPs (located at 522 nm). Meanwhile, the center of the respective Gaussian curve assigned to the silica signal (green line) is slightly red shifted. The last statement agrees with the apparent reduction of the size of the silica spheres when their surface becomes to be covered by Au NPs. These indicatives confirm the increasing Au NPs' content in the composites.

4.2 Effect of metal NPs' load on the SERS EF

Opals with inclusions of Au NPs offer several of the following features: [16, 17, 32]:

- The SERS signal is more intense compared to a disordered template.
- The uniformity/periodicity of the Au NPs' spatial distribution may be controlled by the template.
- A thin layer of Au NPs is enough to increase the SERS signal.
- They are simple and inexpensive to prepare.
- The roughness increases the effective surface of the SERS substrate.
- Less than a milligram of NPs is required to coat a surface of tens of square millimeters.

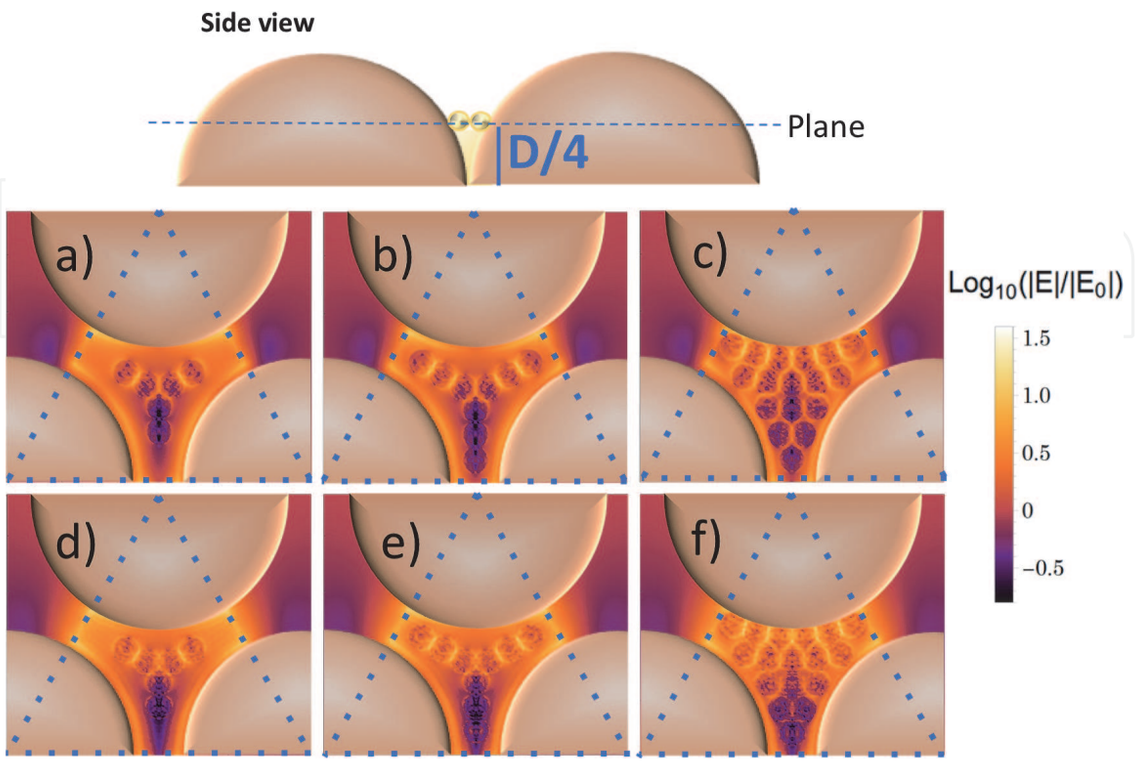

Figure 8.
Electric field intensity of (a) 6, (b) 9, and (c) 17 Au NPs at the intersite of three SiO_2 spheres. The lower panels (d), (e), and (f) are the same systems but with Ag NPs.

The thickness of the colloidal film and load of Au NPs are factors that have been exploited to succeed in the fabrication of an SERS substrate with high qualities. With inverse opal templates, nanoparticle film thickness has proved to have little effect on SERS signal intensity for substrates thicker than a monolayer. On the other hand, opals with Au NPs show a larger enhancement when the film has less than 10 silica layers compared to the thicker ones, and a possible explanation for this is a contribution of multiple scattering within the opal.

Limiting ourselves to the contribution to the SERS enhancement due to the top layer of the composite film, we study the effect of NP concentration. For illustrating low, medium, and high content of metal NPs in the surface layer of the thin film, 6, 9, and 17 metal NPs in the interspace among three dielectric spheres have been considered. An estimation of the single molecule SERS EF can be done through the SERS EF $\approx E^4$ approximation [38], with E being the intensity of the local field. Usually, the size of the metal NPs is one order of magnitude smaller than the size of the dielectric spheres; therefore, we have considered metal NP diameter of 20 nm and SiO_2 dielectric sphere of 200 nm. The spatial configuration of E values for Au and Ag NPs is presented in **Figure 8**. To decrease computational cost, only the area limited by the triangular zone was considered as the target in DDA calculation. The incident EM plane wave is parallel to the plane and travels from left to right, and its wavelength is of 633 nm (red laser). Notice that the SiO_2 spheres apparently are not touching one each other, and the reason is that the plane that is presented is the one that crosses the array as depicted in the side view drawn. In general, the average electric field intensity is of the same order of magnitude for all cases, reaching values 10–12 times the incident electric field, the field being more intense in the spots among NPs, and in the region between the SiO_2 spheres surface and the Au NPs close to it.

5. Conclusions

Along this chapter, we have proved that DDA is a good option to study the optical response of periodic systems. Herein, we use it to model the reflectance and transmittance, at normal incidence, of colloidal films made of SiO_2 spheres with a specific diameter of 200 nm. We show that as the thickness increases from 1 to 12 layers, the center of the photonic band gap shifts to the blue tending to the value of 444 nm. This value is very close to the one corresponding to a 3D opal with HCP structure, 442 nm. Analyzing the trend of the position of the BG, a film with more than eight layers resembles that of a 3D artificial opal. We also compared our results with a 3D artificial opal made with silica spheres of the same size as the one studied by us. We found a good qualitative agreement, and the differences are attributed mainly to the presence of defects in the sample.

Artificial opals with Au NPs are of interest due to their many applications, and one of them is as SERS substrate. A main issue is how to be sure the NPs are being incorporated in the sample. Usually, reflectance spectrum does not show an evident contribution due to the presence of the plasmonic NPs. However, we present here that the absorbance spectrum is wider and asymmetrical compared to the opal without Au NPs. Furthermore, with a deconvolution analysis, it is possible to identify the contribution due to the Au NPs and the silica spheres in the overall spectrum.

For SERS applications, the calculation of electric field intensity gives an idea of the enhancement factor that can be reached by the substrate. At the end of the chapter, we present the spatial distribution of electric field intensity as the amount of metal NPs increases in a monolayer. Taking advantage of the periodicity of the

system, we limited ourselves to the section defined by three silica spheres with N NPs in the void among them. The NPs considered here are one order of magnitude (diameter of 20 nm) smaller than the silica spheres. Therefore, it is possible to host 6, 9, and 17 NPs in the void. Same configuration was used for Au and Ag NPs, finding similar electric field intensities for both of them, about 11 times the incident intensity. But, the spots with these intensities cover a bigger area with Ag NPs than with Au NPs. This indicates that the SERS EF of a specific concentration of molecules would be larger using Ag NPs than Au NPs.

Acknowledgements

The authors thankfully acknowledge the computer resources, technical expertise, and support provided by the Laboratorio Nacional de Supercomputo del Sureste de Mexico, CONACyT network of national laboratories. A.L. González thanks the financial support of Benemerita Universidad Autonoma de Puebla through the VIEP projects GORA-EXC17-G and 100504244-VIEP2018. A. Santos thanks CONACYT by the grant number 258670. M. Toledo Solano thanks support from Mexican National Council for Science and Technology (CONACyT) through Grant A1-S-38743.

Conflict of interest

The authors declare no conflict of interest.

Thanks

Special thanks are given to Dr. Enrique Sánchez, from the Institute of Physics at the Benemerita Universidad Autonoma de Puebla, for his comments and facilities for the synthesis and characterization of the materials presented in **Figures 6** and 7.

Abbreviations

DDA	discrete dipole approximation
NPs	nanoparticles
PBG	photonic band gap
SEM	scanning electron microscopy
FCC	face centered cubic
HCP	hexagonal compact packing
SERS	surface enhanced Raman scattering
EF	enhancement factor
R	reflectance
T	transmittance
EM	electromagnetic

Author details

Ana L. González[1*], Arturo Santos Gómez[1,2] and Miller Toledo-Solano[3]

1 Instituto de Fisica, Benemerita Universidad Autonoma de Puebla, Puebla, Pue., Mexico

2 Instituto Tecnologico Superior de San Martin Texmelucan, San Martin Texmelucan, Puebla, Mexico

3 Facultad de Ciencias Fisico-Matematicas, CONACYT-Benemerita Universidad Autonoma de Puebla, Puebla, Pue., Mexico

*Address all correspondence to: anagr@ifuap.buap.mx

References

[1] Gerasopoulos K, McCarthy M, Royston E, Culver JN, Ghodssi R. Microbatteries with tobacco mosaic virus templated electrodes. In: 2008 IEEE 21st International Conference on Micro Electro Mechanical Systems; IEEE. 2008. pp. 960-963

[2] Atanasova P, Rothenstein D, Schneider JJ, Hoffmann RC, Dilfer S, Eiben S, et al. Virus-templated synthesis of ZnO nanostructures and formation of field? Effect transistors. Advanced Materials. 2011;**23**(42):4918-4922. DOI: 10.1002/adma.201102900

[3] López C. Materials aspects of photonic crystals. Advanced Materials. 2003;**20**:1679-1704. DOI: 10.1002/adma.200300386

[4] García PD, Sapienza R, López C. Photonic glasses: A step beyond white paint. Advanced Materials. 2010; **22**(1):12-19. DOI: 10.1002/adma.200900827

[5] Razo DA, Pallavidino L, Garrone E, Geobaldo F, Descrovi E, Chiodoni A, et al. A version of Stöber synthesis enabling the facile prediction of silica nanospheres size for the fabrication of opal photonic crystals. Journal of Nanoparticle Research. 2008;**10**(7): 1225-1229. DOI: 10.1007/s11051-008-9373-4

[6] Waterhouse GI, Waterland MR. Opal and inverse opal photonic crystals: Fabrication and characterization. Polyhedron. 2007;**26**(2):356-368

[7] Morandi V, Marabelli F, Amendola V, Meneghetti M, Comoretto D. Colloidal photonic crystals doped with gold nanoparticles: Spectroscopy and optical switching properties. Advanced Functional Materials. 2007;**17**(15): 2779-2786. DOI: 10.1002/adfm.200600764

[8] Lu L, Randjelovic I, Capek R, Gaponik N, Yang J, Zhang H, et al. Controlled fabrication of gold-coated 3D ordered colloidal crystal films and their application in surface-enhanced Raman spectroscopy. Chemistry of Materials. 2005;**17**(23):5731-5736. DOI: 10.1021/cm051473d

[9] Nishio M, Moronuki N, Abasaki M. Fabrication of patterned Ag and Au inverse opal structures through repeated self-assembly of fine particles. International Journal of Automation Technology. 2014;**8**(5):755-760. DOI: 10.20965/ijat.2014.p0755

[10] Li W, Xie F, Sun T, Liao Y. Fabrication of gold/silica composite artificial opal by a multiple-step electroplating process. Asia-Pacific Journal of Chemical Engineering. 2008; **3**(3):269-274. DOI: 10.1002/apj.145

[11] Wakayama H, Setoyama N, Fukushima Y. Size-controlled synthesis and catalytic performance of Pt nanoparticles in micro- and mesoporous silica prepared using supercritical solvents. Advanced Materials. 2003; **15**(9):742-745. DOI: 10.1002/adma.200304408

[12] Li H, Wang R, Hong Q, Chen L, Zhong Z, Koltypin Y, et al. Ultrasound-assisted polyol method for the preparation of SBA-15-supported ruthenium nanoparticles and the study of their catalytic activity on the partial oxidation of methane. Langmuir. 2004; **20**(19):8352-8356. DOI: 10.1021/la049290d

[13] Bachan N, Asha A, Jeyarani WJ, Kumar DA, Shyla JM. A comparative investigation on the structural, optical and electrical properties of SiO_2-Fe_3O_4 core-shell nanostructures with their single components. Acta Metallurgica Sinica. 2015;**28**(11):1317-1325. DOI: 10.1007/s40195-015-0328-3

[14] Holtz JH, Asher SA. Polymerized colloidal crystal hydrogel films as intelligent chemical sensing materials. Nature. 1997;**389**(6653):829-832. DOI: 10.1038/39834

[15] Lee YJ, Pruzinsky SA, Braun PV. Glucose-sensitive inverse opal hydrogels: Analysis of optical diffraction response. Langmuir. 2004;**20**(8): 3096-3106. DOI: 10.1021/la035555x

[16] Kuncicky DM, Prevo BG, Velev OD. Controlled assembly of SERS substrates templated by colloidal crystal films. Journal of Materials Chemistry. 2006; **16**(13):1207-1211. DOI: 10.1039/ B512734C

[17] Tsvetkov MY, Khlebtsov BN, Khanadeev VA, Bagratashvili VN, Timashev PS, Samoylovich MI, et al. SERS substrates formed by gold nanorods deposited on colloidal silica films. Nanoscale Research Letters. 2013; **8**(1):250. DOI: 10.1186/1556-276X-8-250

[18] González AL, Noguez C. Influence of morphology on the optical properties of metal nanoparticles. Journal of Computational and Theoretical Nanoscience. 2007;**4**(2):231-238. DOI: 10.1166/jctn.2007.2309

[19] Noguez C, Villagómez CJ, González AL. Plasmonics of multifaceted metallic nanoparticles, field enhancement, and TERS. Physica Status Solidi (B). 2015;**252**(1):56-71. DOI: 10.1002/pssb.201350416

[20] Yurkin MA, Semyanov KA, Tarasov PA, Chernyshev AV, Hoekstra AG, Maltsev VP. Experimental and theoretical study of light scattering by individual mature red blood cells by use of scanning flow cytometry and a discrete dipole approximation. Applied Optics. 2005;**44**(25):5249-5256. DOI: 10.1364/AO.44.005249

[21] Bronk BV, Druger SD, Czege J, Van de Merwe WP. Measuring diameters of rod-shaped bacteria in vivo with polarized light scattering. Biophysical Journal. 1995;**69**(3):1170-1177. DOI: 10.1016/S0006-3495(95)79991-X

[22] Draine BT. The discrete-dipole approximation and its application to interstellar graphite grains. The Astrophysical Journal. 1988;**333**: 848-872. DOI: 10.1086/166795

[23] Lazarides AA, Kelly KL, Schatz GC. Effective medium theory of DNA-linked gold nanoparticle aggregates: Effect of aggregate shape. MRS Online Proceedings Library Archive. 2001;**635**. DOI: 10.1557/PROC-635-C6.5

[24] Draine BT, Flatau PJ. Discrete-dipole approximation for periodic targets: Theory and tests. JOSA A. 2008; **25**(11):2693-2703. DOI: 10.1364/ JOSAA.25.002693

[25] Santos Gómez A, González AL. Far field optical properties of a monolayer of SiO_2 spheres and small Au nanoparticles. MRS Advances. 2018; **3**(64):3917-3923. DOI: 10.1557/ adv.2019.128

[26] DDSCAT code. User guide, download options and more are available from: http://ddscat.wikidot.com [Accessed: 2019-08-02]

[27] Bohren CF, Huffman DR. Absorption and Scattering of Light by Small Particles. Wiley-VCH; 1998. 530 p. DOI: 10.1002/9783527618156

[28] Malitson IH. Interspecimen comparison of the refractive index of fused silica. JOSA. 1965;**55**(10): 1205-1209. DOI: 10.1364/ JOSA.55.001205

[29] Brixner B. Refractive-index interpolation for fused silica. JOSA. 1967;**57**(5):674-676. DOI: 10.1364/ JOSA.57.000674

[30] Braun MM, Pilon L. Effective optical properties of non-absorbing nanoporous thin films. Thin Solid Films.

2006;**496**(2):505-514. DOI: 10.1016/j.tsf.2005.08.173

[31] Vos WL, Sprik R, van Blaaderen A, Imhof A, Lagendijk A, Wegdam GH. Strong effects of photonic band structures on the diffraction of colloidal crystals. Physical Review B. 1996; **53**(24):16231. DOI: 10.1103/PhysRevB.53.16231

[32] Romero-Cruz LA, Santos-Gómez A, Palomino-Ovando MA, Hernández-Cristobal O, Sánchez-Mora E, González AL, et al. Surface enhanced Raman scattering due to interstitial gold nanoparticles into SiO_2 spheres array. Superlattices and Microstructures. 2018; **123**:71-80. DOI: 10.1016/j.spmi.2018.02.022

[33] Stöber W, Fink A, Bohn E. Controlled growth of monodisperse silica spheres in the micron size range. Journal of Colloid and Interface Science. 1968;**26**(1):62-69. DOI: 10.1016/0021-9797(68)90272-5

[34] Turkevich J, Stevenson PC, Hillier J. A study of the nucleation and growth processes in the synthesis of colloidal gold. Discussions of the Faraday Society. 1951;**11**:55-75. DOI: 10.1039/DF9511100055

[35] Kimling J, Maier M, Okenve B, Kotaidis V, Ballot H, Plech A. Turkevich method for gold nanoparticle synthesis revisited. The Journal of Physical Chemistry B. 2006;**110**(32):15700-15707. DOI: 10.1021/jp061667w

[36] Cong H, Yu B. Fabrication of superparamagnetic macroporous Fe3O4 and its derivates using colloidal crystals as templates. Journal of Colloid and Interface Science. 2011;**353**(1):131-136. DOI: 10.1016/j.jcis.2010.09.040

[37] Carmona-Carmona AJ, Palomino-Ovando MA, Hernández-Cristobal O, Sánchez-Mora E, Toledo-Solano M. Synthesis and characterization of magnetic opal/Fe_3O_4 colloidal crystal. Journal of Crystal Growth. 2017;**462**:6-11. DOI: 10.1016/j.jcrysgro.2016.12.105

[38] Le Ru E, Etchegoin P. Principles of Surface-Enhanced Raman Spectroscopy and Related Plasmonic Effects. 1st ed. Amsterdam: Elsevier; 2009. p. 688